JOURNAL OF MATERIALS SCIENCE 31 (1996) 5373–5383

Tensile testing and TEM analysis of nitrogen-strengthened Fe–Ni–Cr single crystals

X. W. ZHOU, M. GRUJICIC*
Department of Mechanical Engineering, Center for Advanced Manufacturing, Clemson University, Clemson, SC 29634, USA

A conventional "abnormal grain growth annealing" heat treatment has been used to produce low (0.009 wt %) and high (0.12 wt %) nitrogen single crystalline Fe–40Ni–15Cr wt % base alloys. Constant strain-rate tensile tests were carried out in the temperature range between 77 and 298 K at two different strain-rates. The results obtained were analysed using the standard procedure for the thermally activated glide of dislocations, and the possible rate-controlling mechanisms for athermal and thermal nitrogen-induced strengthening have been discussed. A conventional two-beam bright-field transmission electron microscope was next used to determine the character of the dislocations and their dependence on the amount of nitrogen in the alloy. It was found that the dislocations became predominantly screw in character as the nitrogen content in the alloy was increased. These findings have been discussed in the light of the existing models for the nitrogen strengthening of the Fe–Ni–Cr austenite.

1. Introduction

A number of previous studies on polycrystalline Fe–Ni–Cr base alloys [1–7] revealed that the presence of nitrogen in these alloys is associated with several important effects. These can be summarized as follows: (1) the strength increase due to nitrogen is exceptionally high compared to what can be expected from the interstitial solid-solution strengthening of the f c c alloy systems [1, 2]; (2) the increase in yield stress with a decrease in temperature at subambient temperatures is substantially larger compared to its counterpart in a typical f c c alloy and in fact approaches that observed in the b c c alloys [3]; (3) planar slip is promoted in the alloys containing nitrogen, even when the amount of nitrogen is as small as 0.03 wt % [1, 3–7]; and (4) accompanying planar slip is the occurrence of straight dislocations having an almost exclusively screw character [1, 5]. Most of these effects cannot be accounted for using the conventional continuum models for solid-solution strengthening (e.g. [1]). On the other hand, our recent work based upon the use of atomistic simulations of the nitrogen-dislocation interactions [8–10] and the analysis of the short-range order and its effect on the plastic flow behaviour [11], suggests that the nitrogen-induced effects can be explained, at least qualitatively. To carry out a more quantitative comparison between the theoretical predictions and the experiments, experimental data for the Fe–Ni–Cr–(N) single crystalline alloys are required because the models discussed [8–11] pertain to single crystalline materials. Our literature search revealed no experimental data for Fe–Ni–Cr–(N) single crystals which could be used to test the models.

The objective of the present work was to prepare two Fe–Ni–Cr base single crystalline materials, one containing no nitrogen (beyond the trace amounts), and the other containing a significant amount of nitrogen. These two alloys were then studied using tensile testing and transmission electron microscopy (TEM) in order to generate the experimental data necessary to understand better the role of nitrogen in the Fe–Ni–Cr austenite.

2. Experimental procedure

2.1. Preparation of single crystalline tensile specimens

The starting material used in the present work was a polycrystalline Fe–40Ni–15Cr (wt %) alloy whose chemical composition is given in Table I. The polycrystalline alloy was produced by ingot casting in the Materials Processing Laboratory of Sandvic A.B., Sweden. After casting, the material was forged into 87 mm diameter bars at temperatures between 1220 and 1240 °C, machined into 77 mm diameter × 200 mm length rounds, and extruded into 15 mm diameter rods at 1180–1190 °C. To prepare the strips from which flat tensile specimens can be machined, rectangular work pieces (~ 15 mm × 5.8 mm × 100 mm) were first cut from the 15 mm diameter rods. The pieces were next cold rolled into strips approximately 3.3 mm thick and annealed at 1000 °C for 1 h. To minimize the contamination of the alloy, the

* Author to whom all correspondence should be addressed.

0022–2461

TABLE I The chemical compositions (wt %) of the polycrystalline Fe–40Ni–15Cr wt % alloy used in the present work

C	Si	Mn	P	S	Cr	Ni	Mo	Al	Mg	O p.p.m.	N
0.011	0.28	0.10	0.005	≤ 0.003	14.6	39.7	< 0.01	0.033	0.023	$31 \sim 39$	0.009

annealing was carried out in an ultra-high purity (UHP) argon gas atmosphere. To produce single crystalline specimens of the Fe–40Ni–15Cr (wt %) alloy, we employed the technique based on the abnormal grain-growth annealing which is frequently used for metallic materials with a high melting point [12]. To obtain an initial fine-grained fully recrystallized microstructure which is a prerequisite for a successful abnormal grain-growth annealing heat treatment, the 3.3 mm thick strips were cold rolled down to ~ 1 mm ($\sim 70\%$ thickness reduction), and subsequently annealed at 1000 °C for 1 h in the UHP argon gas. The flat 10 mm gauge length tensile specimens were next machined from the 1 mm thick strips, prestrained in tension by about 6%, and then rapidly heated up to 1300 °C and kept at this temperature for 100 h under UHP argon in the Centorr Vacuum/Inert Gas Furnace. This procedure typically resulted in a single grain covering the entire gauge length of the specimens and several grains occupying the specimen shoulders.

Our thermodynamic analysis using the THERMOCALC computer program [13] showed that in the Fe–40Ni–15Cr wt % base alloy, the chemical potential of nitrogen corresponding to a concentration of ~ 0.12 wt % is in equilibrium with pure gaseous nitrogen at 1.2 atm pressure and 1250 °C. Hence, to obtain the single crystalline alloy with a high nitrogen content (0.12 wt %), we carried out a 1250 °C/24 h heat treatment in UHP nitrogen at 1.2 atm pressure. Subsequent chemical analysis showed that this heat treatment indeed yielded a nitrogen content in the alloy of ~ 0.12 wt %. Using the function $D = (10^{-0.04} \times 10^{-8800/T})\ \mathrm{cm^2\,s^{-1}}$ for the nitrogen diffusivity in austenite [14], the diffusion distance for nitrogen after the nitriding period, $t = 24$ h, is estimated as $s = (Dt)^{1/2} \approx 3.6$ mm. Because this distance significantly exceeds the specimen half thickness (≈ 0.5 mm), one can assume that the equilibrium nitrogen concentration was achieved throughout the entire specimen.

To summarize, the procedure employed yielded two Fe–40Ni–15Cr (wt %) base single crystals: one with a low (0.009 wt %) nitrogen content subsequently referred as S1 alloy, and the one with a high (0.12 wt %) nitrogen content subsequently referred to as S2 alloy.

2.2. Determination of the orientation of single crystals

To obtain the Schmid factor which is necessary for determination of the critical shear stress for the onset of plastic deformation, the load direction for each of the tensile specimens used had to be determined. In the present work, we employed a method which requires the use of a transmission electron microscope to determine the crystallographic character of the load direction in the single crystalline tensile specimen. The method involves the following steps. First, the load direction is denoted (by placing fiduciary marks) on the opposite edges (along the diameter) of the 3 mm diameter TEM specimen cut from the tensile specimen. Such marks remain visible after thinning the TEM specimens through the use of double jet polishing. Finally, when the specimen is mounted in the TEM specimen holder, it is oriented in such a way that the load direction (the fiduciary marks) is aligned parallel to one of the two sample tilting axes of the holder. To determine the load direction, a number of diffraction patterns corresponding to different tilting angles about the tilting axis parallel to the load direction are obtained while keeping the rotation about the other sample tilting axis at zero. Following the procedure for the TEM data analysis [8], the corresponding beam direction $\boldsymbol{B}$ (reverse of the direction of electron beam), is determined for each of the diffraction patterns. Because the beam direction, $\boldsymbol{B}$, is always perpendicular to the sample tilting axis, or the load direction, $\boldsymbol{P}$, in the present case, the cross-product of the two beam directions is used to define the load direction, $\boldsymbol{P}$. Using the method, the load direction could be determined within an accuracy of $\pm 3°$.

2.3. Mechanical testing

The mechanical tensile testing of the specimens was carried out using a servohydraulic Instron 8000 mechanical testing machine equipped with a 66750 Newton capacity load cell. Two sets of mechanical tests were conducted. To study the thermally activated nature of the strengthening by nitrogen, the first set of tests was conducted at five temperatures (77, 170, 200, 220, and 298 K) and crosshead speeds corresponding to two shear strain rates (1.089×10^{-3} and $1.089 \times 10^{-2}\ \mathrm{s^{-1}}$) for both the S1 and S2 specimens. The subambient testing temperatures were achieved by carrying out the tests in either liquid nitrogen or in a mixture of liquid nitrogen and methanol. In order to minimize the influence of the errors associated with the determination of the orientation of the loading direction of the single crystalline tensile specimen on the results and reduce the amount of work spent on producing single crystals, one specimen was tested under more than one testing condition. Towards that end, the tensile tests were stopped as soon as the plastic deformation was observed. The "deformed" specimens were next annealed in an UHP gas using the following heat treatment: 100 °C/2 h + 200 °C/2 h + 300 °C/2 h + 400 °C/2 h, and then reused for testing at other temperatures and/or crosshead speeds. To verify that this procedure did not introduce a systematic change in yield stress, we retested the specimen at the same condition after several intermediate

tests at different testing conditions, and found no significant change in the magnitude of yield stress. The 0.2% offset yield stress, $\sigma_{0.2}$, was determined in each case from the tensile stress versus tensile strain curves following the standard procedure. The critical shear stress for the onset of plastic deformation was then calculated by multiplying the $\sigma_{0.2}$ with the corresponding Schmid factor.

The second set of tests was used to reveal the effect of nitrogen on the strain-hardening rate of single crystalline specimens of the alloys. The specimens S1 and S2 were tested at one temperature (77 K) and one crosshead speed (0.00476 mm s^{-1}) until fracture.

2.4. TEM observation of dislocations

The dislocation character and the substructure in the single crystalline Fe–40Ni–15Cr wt % base austenites with a low (alloy S1) and a high (alloy S2) nitrogen concentration were determined using the conventional two-beam bright-field transmission electron microscopy (TEM) technique. The work was done using a Hitachi 600 AB transmission electron microscope operating at 100 kV. The tensile specimens tested to small strains ($\varepsilon < 2\%$) at 77 K temperature and 0.00476 mm s^{-1} crosshead speed were mechanically thinned into 0.03 mm thick foil and punched out into 3 mm diameter discs, which were further thinned until perforation using the standard double-jet electropolishing technique. A mixture of 10 vol % perchloric acid and 90 vol % methanol, cooled to −40 °C, was used as the electrolyte for the double-jet polishing. The polishing voltage was 15 V.

3. Results

3.1. Mechanical testing

In order to be able to relate the experimental findings with the model predictions, it was necessary to convert the tensile stress and tensile strain into their shear counterparts. This was done as follows.

As explained earlier, the shear stress can be obtained by multiplying the tensile stress with the appropriate value of the Schmid factor. Considering the rotation of the crystallographic planes during tensile testing, the relation between the shear strain, γ, and the tensile strain, ε, of a single crystal can be expressed as [15]

$$\gamma = \frac{1}{\cos\phi_0}\{[(1+\varepsilon)^2 - \sin^2\lambda_0]^{1/2} - \cos\lambda_0\} \quad (1)$$

where ϕ_0 and λ_0 are respectively, the initial angle between the load direction and the slip plane normal, and the initial angle between the load direction and the slip direction. Angles ϕ_0 and λ_0 had different values in the different specimens.

After differentiating Equation 1 with respect to time, one obtains the relation between shear strain rate, $\dot{\gamma}$, and normal strain rate, $\dot{\varepsilon}$

$$\dot{\gamma} = \frac{(1+\varepsilon)\dot{\varepsilon}}{\cos\phi_0[(1+\varepsilon)^2 - \sin^2\lambda_0]^{1/2}} = \frac{(1+\varepsilon)V}{\cos\phi_0[(1+\varepsilon)^2 - \sin^2\lambda_0]^{1/2}L} \quad (2)$$

where V is the crosshead speed, and L the gauge length of the specimens. At the onset of plastic deformation, the contribution of plastic tensile strain, ε, to Equation 2 can be neglected ($\varepsilon \sim 0.002 \ll 1$). It should be noted that for each specimen having particular values of ϕ_0 and λ_0, the crosshead speed was determined using Equation 2 so that one of the two constant shear strain rates, $\dot{\gamma}_1 = 1.089 \times 10^{-3}\ s^{-1}$, and $\dot{\gamma}_2 = 1.089 \times 10^{-2}\ s^{-1}$, is obtained. Following the procedure just described, the (tensile) yield stress versus temperature data in our first set of tests were converted into the (critical) shear stress versus temperature curves (at a constant shear strain rate), and the results are summarized in Fig. 1.

Next the well-established procedure for the analysis of thermally activated motion of dislocations [1, 16, 17], was utilized to decompose the critical shear stress for the onset of plastic deformation into its athermal and thermal components. Under the assumption that the thermal and athermal strengthening mechanisms are associated with very different characteristic length scales, the athermal component of the critical shear stress, τ_a, and the thermally activated one, τ_{th}, can be considered as linearly additive, i.e.

$$\tau_c = \tau_a + \tau_{th} \quad (3)$$

Typically, the athermal component of the critical shear stress, τ_a, is determined by equating it with the experimental critical shear stress at the temperatures which are sufficiently high so that the thermal component of the shear stress is negligible. Using the high-temperature value for τ_a and the fact that τ_a scales with the shear modulus of the alloy, which is readily available [1], one can evaluate the athermal shear stress at lower temperatures. Because the shear modulus increases moderately and linearly (at least within a narrow temperature range) with decreasing temperature, the athermal component of the critical shear stress, τ_a, increases moderately and linearly with decreasing temperature [1]. The thermal component of the critical shear stress, τ_{th}, at lower temperatures can then be calculated, in accordance with Equation 3, by simply deducting τ_a from the experimental critical shear stress, τ_c.

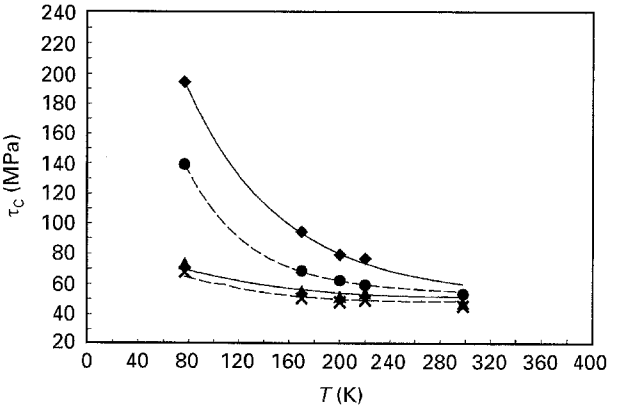

Figure 1 The critical shear stress, τ_c, as a function of temperature at two shear strain rates in the Fe–40Ni–15Cr wt % base single crystalline alloys with low (S1) and a high (S2) nitrogen concentration. (▲, ×) S1, (◆, ●) S2, (———) $\dot{\gamma} = 1.089 \times 10^{-2}\ s^{-1}$, (– – –) $\dot{\gamma} = 1.089 \times 10^{-3}\ s^{-1}$.

The experimental τ_c versus T curves, Fig. 1, associated with two different shear strain rates $\dot{\gamma}_1 = 1.089 \times 10^{-3}\ s^{-1}$ and $\dot{\gamma}_2 = 1.089 \times 10^{-2}\ s^{-1}$, are fitted using the least squares procedure, to a function τ_c (MPa) $= Ae^{-BT} + CT + D$, where temperature T is in K. The results of this fitting procedure are shown in Table II.

A careful examination of Fig. 1 suggests that the thermal stress in the S1 alloy is negligible at temperatures above 233 K, and thus the experimental critical shear stress in this alloy, is equated with the athermal shear stress between 233 and 298 K, and is fitted with a linear function in the form

$$\tau_a = -0.022\,50T + 52.13 \quad \text{(MPa)} \tag{4}$$

Because nitrogen does not change the shear modulus significantly [1], the temperature dependence of the athermal shear stress found in the S1 alloy is assumed also to hold for the S2 alloy in accordance with the assumption that the athermal stress scales with the corresponding shear modulus. This procedure yielded the following temperature dependence of the athermal shear stress in the S2 alloy

$$\tau_a = -0.022\,50T + 59.51 \quad \text{(MPa)} \tag{5}$$

The temperature dependence of the shear modulus in the polycrystalline Fe–40Ni–15Cr wt % alloy was reported to be $-0.045\%\ K^{-1}$ [1]. The temperature dependence of the athermal stress represented by Equations 4 and 5 is assessed as $\sim -0.050\%\ K^{-1}$. The closeness of the two values confirm that the temperature dependence of the athermal stress is dominated by the temperature dependence of the shear modulus.

The thermal component of the shear stress is next obtained by subtracting the athermal component from the experimental critical shear stress, and is given by a function τ_{th}(MPa) $= Ae^{-BT} + CT + D$, where the coefficients A, B, C, and D are given in Table III.

Following the procedure for the analysis of the thermally activated glide of dislocation, one needs to determine the activation volume which is defined as

$$V = k_B T \left(\frac{\partial \ln \dot{\gamma}}{\partial \tau_{th}}\right)_T \approx k_B T \left(\frac{\Delta \ln \dot{\gamma}}{\Delta \tau_{th}}\right)_T$$

$$= 13.8T \left(\frac{\Delta \ln \dot{\gamma}}{\Delta \tau_{th}}\right)_T \quad (nm^3)$$

$$= \frac{13.8T}{\Omega} \left(\frac{\Delta \ln \dot{\gamma}}{\Delta \tau_{th}}\right)_T \quad \text{(atomic volumes)} \tag{6}$$

TABLE II Coefficients A, B, C, and D in the function $\tau_c = Ae^{-BT} + CT + D$

Alloy	Strain rate (s^{-1})	A	B	C	D
S1	1.089×10^{-3}	62.91	−0.009 10	0.048 05	29.68
	1.089×10^{-2}	64.58	−0.007 51	0.048 05	29.68
S2	1.089×10^{-3}	404.22	−0.020 81	−0.022 50	59.51
	1.089×10^{-2}	398.38	−0.013 90	−0.022 50	59.51

where k_B is the Boltzmann constant, T the temperature, Ω (nm^3) the atomic volume ($\Omega = a^3/4$ for the f c c crystal), and $\Delta \ln \dot{\gamma}$ and $\Delta \tau_{th}$ (MPa) are, respectively, the $\ln \dot{\gamma}$ and τ_{th} increments. Based upon the τ_{th} versus T functions given in Table III, the activation volume was calculated as a function of the thermal stress using Equation 6. The results of this calculation are represented in Fig. 2 as a τ_{th} versus V plot, which is commonly referred to as the obstacle profile.

Next, the τ_{th} versus T functions at two different shear strain rates (Table III) were used to determine the activation energy as a function of the thermal stress according to the following equation

$$H = -\left[\frac{\partial \ln \dot{\gamma}}{\partial_{(k_B T)^{-1}}}\right]_{\tau_{th}} \approx -k_B \left(\frac{\Delta \ln \dot{\gamma}}{\Delta T^{-1}}\right)_{\tau_{th}}$$

$$= -8.63 \times 10^{-5} \left(\frac{\Delta \ln \dot{\gamma}}{\Delta T^{-1}}\right)_{\tau_{th}} \quad \text{(eV)} \tag{7}$$

The results of this calculation are shown in Fig. 3. Kocks *et al.* [16] pointed out that for many models of thermally activated plastic flow, the activation energy can be represented by the following phenomenological formula

$$H = H_0 \left[1 - \left(\frac{\tau_{th}}{\hat{\tau}_{th}}\right)^p\right]^q \tag{8}$$

where H_0 is the maximum activation energy corresponding to the condition $\tau_{th} = 0$, $\hat{\tau}_{th}$ the maximum

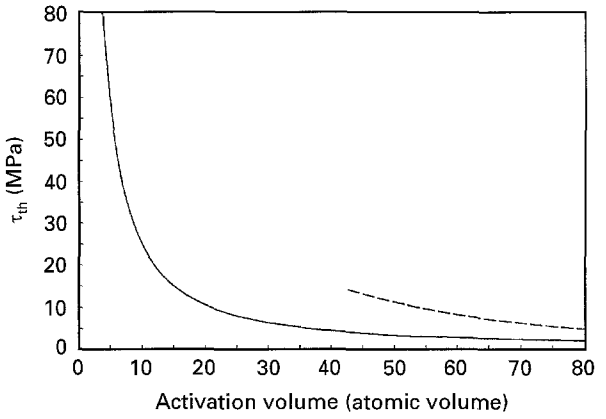

Figure 2 The obstacle profile for the (---) S1 and (——) S2 single crystalline alloys.

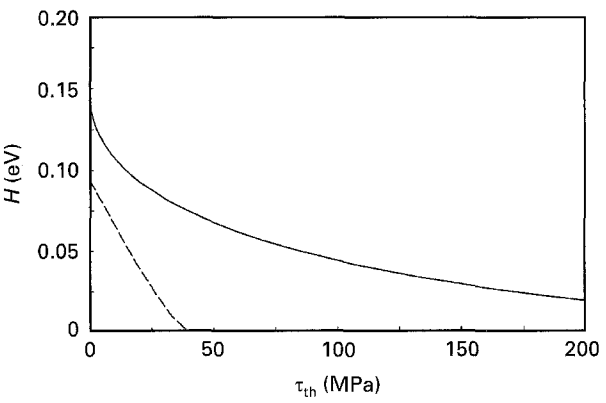

Figure 3 Activation energy of thermally activated plastic flow as a function of the thermal component of the critical shear stress. (---) S1, (——) S2.

(threshold) thermal stress beyond which no thermal activation is needed for the motion of dislocations, and p and q are the parameters which take on characteristic values for each particular thermally activated rate-controlling mechanism of dislocation motion. Based on the results given in Table III, the average value of the threshold thermal stress was determined as $\hat{\tau}_{th} = \tau_{th}|_{T=0}$. By fitting Equation 8 to the H versus τ_{th} data shown in Fig. 3, the values of H_0, p, and q were determined and the results are listed in Table IV.

The results of the second set of tensile tests, showing the entire shear stress versus shear strain curves in the two alloys, are given in Fig. 4. The addition of nitrogen clearly enhances the strength and somewhat the rate of strain hardening, without affecting the ductility significantly.

3.2. Determination of dislocation character

A typical dislocation configuration observed in the S1 alloy containing a low nitrogen concentration is shown in Fig. 5. It is apparent in Fig. 5 that there is no preferred orientation for the line direction of the dislocations. According to our atomistic simulation results of the dislocation core structure [8–10], the stacking fault width in the Fe–40Ni–15Cr wt % base alloy is less than 8 nm. Hence, the individual Shockley partial dislocations resulting from the dissociation of a unit $\frac{a}{2}\langle 1\,1\,0\rangle$ dislocation are not expected to be resolved by the conventional two-beam bright-field TEM technique at the maximum available magnification of $\times$ 53000. This explains why the individual partial dislocations are not revealed in Fig. 5. It is customary to analyse the dislocations whose dissociated core structure is not resolved by the conventional TEM technique as if they were the unit dislocations, and this approach was adopted in the present work. Along this line, because in an fcc crystal there are six possible $\frac{a}{2}\langle 1\,1\,0\rangle$ type Burgers vectors for a unit dislocation, the random distribution of dislocation line directions seen in Fig. 5 suggests that the dislocations are predominantly of the mixed type, with varying contributions of their edge and screw components.

TABLE III Coefficients A, B, C, and D in the function $\tau_{th} = Ae^{-BT} + CT + D$

Alloy	Strain rate (s^{-1})	A	B	C	D
S1	1.089×10^{-3}	62.91	−0.009 10	0.070 55	−22.45
	1.089×10^{-2}	64.58	−0.007 51	0.070 55	−22.45
S2	1.089×10^{-3}	404.22	−0.020 81	0	0
	1.089×10^{-2}	398.38	−0.013 90	0	0

TABLE IV Thermal activation parameters H_0, $\hat{\tau}_{th}$, p, and q in Equation 8

Alloy designations	H_0(eV)	$\hat{\tau}_{th}$ (MPa)	p	q
S1	0.094	41.30	1.08	1.43
S2	0.154	401.30	0.43	1.60

Contrary to the random distribution of mixed type dislocations in the S1 alloy with a low nitrogen concentration, the dislocation substructure in the S2 alloy containing a high nitrogen concentration was found to be dominated by long arrays of parallel dislocations. An example of such a dislocation array is displayed in Fig. 6a. In addition to the long dislocation arrays, shorter dislocation arrays composed of two to five dislocations were occasionally observed and these short arrays were found to intersect with the long arrays, as shown in Fig. 6b. An example of the long dislocation array is marked "A", while a short array is marked "B" in Fig. 6b. A systematic observation of the long and short dislocation arrays from different directions confirmed that they are all associated with planar slip, i.e. they consist of parallel dislocations gliding on the same slip plane.

The formation of the dislocation arrays is apparently related to the presence of a high concentration of nitrogen because similar arrays were not observed in the S1 alloy with a low concentration of nitrogen. To elucidate the role of nitrogen in the formation dislocation arrays, we proceeded with the determination of the character of the dislocations in the arrays. Toward that end, the dislocation configuration shown in Fig. 6b was imaged under three additional diffracting conditions, and the results are shown, respectively, in

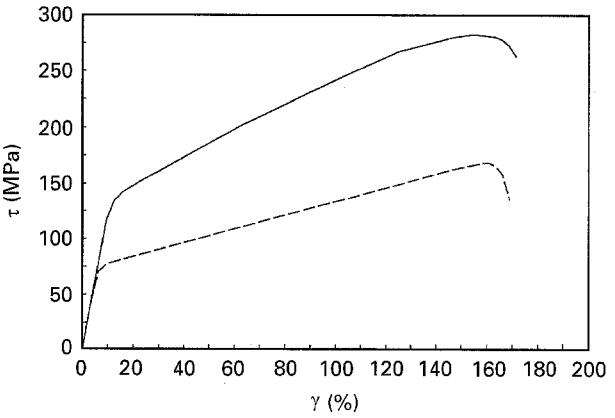

Figure 4 Shear stress versus shear strain curves obtained in the second set of tests. (– – –) S1, (——) S2, $\dot{\gamma} = 1.089 \times 10^{-3}\,s^{-1}$, $T = 77$ K.

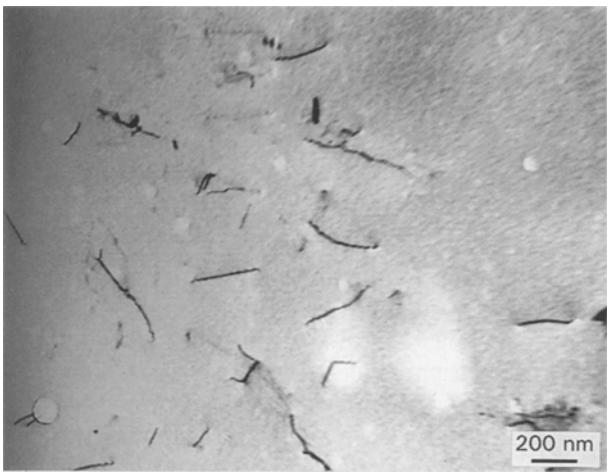

Figure 5 Typical dislocation configuration in the S1 alloy with a low nitrogen concentration ($\varepsilon \approx 2\%$), $\boldsymbol{g} = (\bar{1}\,1\,1)$.

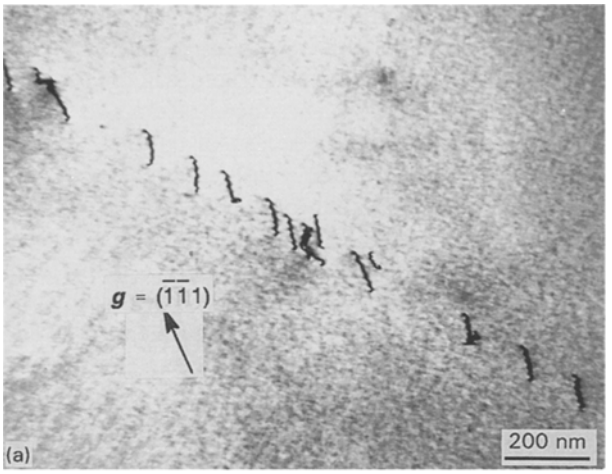

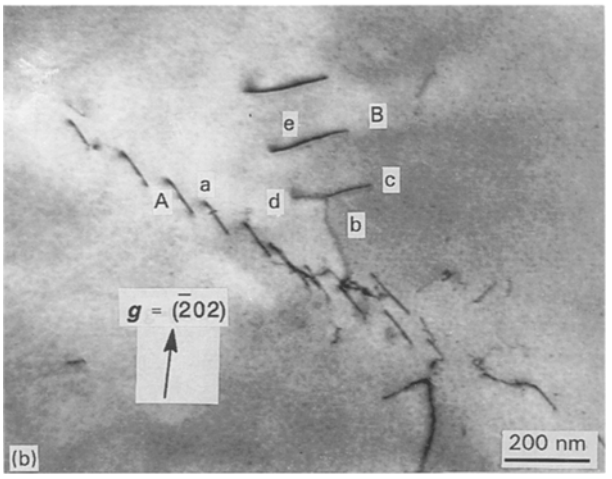

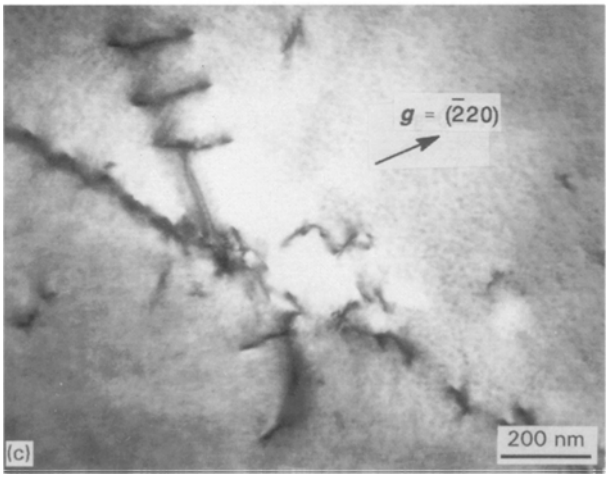

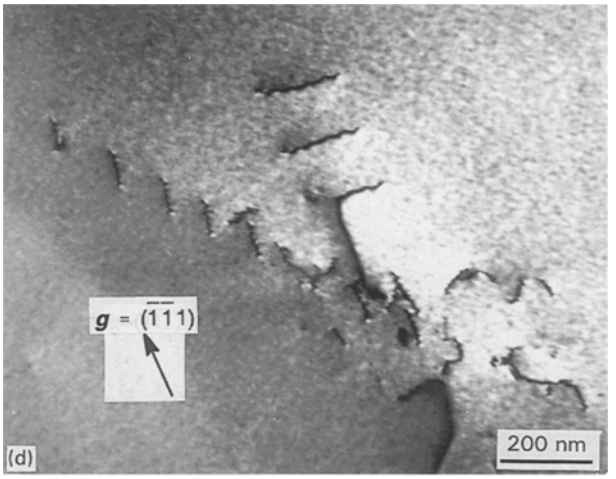

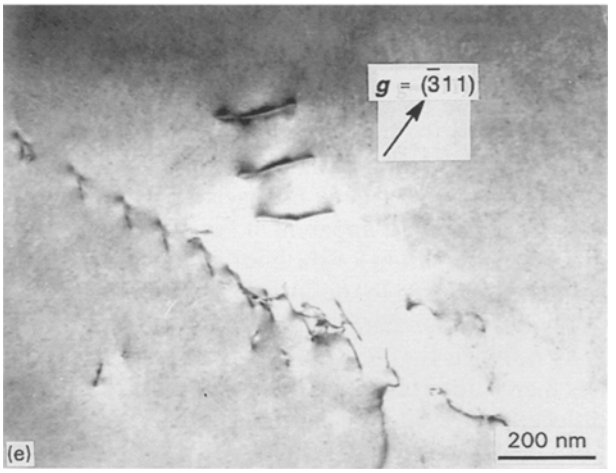

Figure 6 Dislocation configuration in the S2 alloy with a high nitrogen concentration ($\varepsilon \approx 2\%$) under the five imaging conditions: (a) $\boldsymbol{B} \approx [1\,1\,2]$, $\boldsymbol{g} = (\bar{1}\,\bar{1}\,1)$; (b) $\boldsymbol{B} \approx [1\,1\,1]$, $\boldsymbol{g} = (\bar{2}\,0\,2)$; (c) $\boldsymbol{B} \approx [1\,1\,1]$, $\boldsymbol{g} = (\bar{2}\,2\,0)$; (d) $\boldsymbol{B} \approx [1\,1\,2]$, $\boldsymbol{g} = (\bar{1}\,\bar{1}\,1)$; and (e) $\boldsymbol{B} \approx [1\,1\,2]$, $\boldsymbol{g} = (\bar{3}\,1\,1)$.

TABLE V The visibility conditions for five types of dislocations a, b, c, d, and e marked in Fig. 6b associated with four different diffracting vectors $\boldsymbol{g}$

Dislocations	Diffracting vector, $\boldsymbol{g}$			
	$\bar{2}02$	$\bar{2}20$	111	$\bar{3}11$
a	Visible	Invisible	Visible	Visible
b	Visible	Visible	Visible	Invisible
c	Visible	Visible	Visible	Visible
d	Visible	Visible	Invisible	Visible
e	Visible	Visible	Visible	Visible

Fig. 6c–e. Following the standard procedure for the analysis of TEM data [8], the diffracting vector $\boldsymbol{g}$ and its relation to the corresponding image were determined and indicated for each of the dislocation images displayed in Fig. 6a–e. The beam direction, $\boldsymbol{B}$, indicated in Fig. 6a–e refers to the approximate beam direction, i.e. to the direction of the corresponding low index prominent zone axis.

As mentioned earlier, due to the inability of the two-beam bright-field transmission electron microscope to resolve the individual partial dislocations, the dislocations revealed in Fig. 6b–e are analysed as if they were unit $\frac{a}{2}\langle 1\,1\,0\rangle$ dislocations.

Careful examination of Fig. 6b indicates that there are five different dislocation types: dislocation a (one of the dislocations in the array A), and dislocations b, c, d and e in the array B. In addition, dislocations b, c and d form a node at their intersection point and are found not to reside on the same slip plane. The Burgers vectors for each of these dislocations are determined using four two-beam bright-field images displayed in Fig. 6b–e. The visibility conditions for the five types of dislocations under the four different diffracting conditions employed in Fig. 6b–e are summarized in Table V.

Under the assumption that the dislocations are of the $\frac{a}{2}\langle 1\,1\,0\rangle$ type, the results shown in Table V are

used to determine the Burgers vectors according to the dislocation invisibility criteria [8, 18, 19]. The Burgers vectors of dislocations a, b, c and e were determined respectively as: $\boldsymbol{b}_a = \pm\frac{a}{2}[1\,1\,0]$, $\boldsymbol{b}_b = \pm\frac{a}{2}[0\,\bar{1}\,1]$, $\boldsymbol{b}_c = \boldsymbol{b}_e = \pm\frac{a}{2}[1\,0\,\bar{1}]$. For dislocation d, however, there are two possible Burgers vectors, $\pm\frac{a}{2}[1\,\bar{1}\,0]$ and $\pm\frac{a}{2}[0\,1\,1]$. Because dislocations b, c, and d form a node, the sum of their Burgers vectors must be zero. This condition allows the Burgers vector of dislocation d to be determined as $\boldsymbol{b}_d = \pm\frac{a}{2}[1\,\bar{1}\,0]$.

To determine the line direction of dislocations a, b, c, d, and e, two TEM images shown in Fig. 6b and d, each corresponding to a different beam direction, were used. The two-beam conditions corresponding to Fig. 6b and d were obtained by slightly tilting the specimens from the symmetric condition of the respective prominent low-index diffraction pattern. The zone axes of the two prominent low-index diffraction patterns are, respectively, [1 1 1] and [1 1 2]. Using our TEM image analysis programme [8], the two beam directions used in Fig. 6b and d are determined as [17 19 17] and [8 7 16], respectively. As expected, they are respectively close to the [1 1 1] and [1 1 2] directions.

The slip plane normal for a dislocation can be determined using a number of methods such as (a) obtaining the cross-product of the dislocation line direction and its Burgers vector (for non-screw dislocations only); (b) taking the cross-product of the line directions of two non-parallel dislocations on the same slip plane; (c) taking the cross-product of one dislocation line direction and another line direction lying on the same slip plane (e.g. the line joining the midpoints of two dislocations lying on the same slip plane, or the line connecting the end of the one dislocation to the midpoint of another dislocation on the same slip plane), etc. In the present work, these methods were complemented by the condition that, because the alloy tested has the f c c structure, the slip plane for each of the dislocations analysed must be one of the $\{1\,1\,1\}$ planes. To determine which of the $\{1\,1\,1\}$ planes is the slip plane for a given dislocation, the dislocation line direction and the direction of another line on the same slip plane were first determined using the TEM image analysis programme [8]. The cross-product of the two directions was next calculated and the result replaced by the nearest $\langle 1\,1\,1\rangle$ slip plane normal. Finally the dislocation line direction was recomputed using the same programme [8] under the condition that the line direction lies on the slip plane already determined. The result of this procedure are listed in Table VI. Also indicated in this table is the acute angle, α, between the dislocation line direction and the corresponding Burgers vector, which can be used to determine the character of the dislocation.

It can be seen from Table VI that all the dislocations are of the mixed type. However, dislocation a is nearly of the screw type while dislocations c and e are close to the edge type. In addition, it can be seen that dislocations c and e belong to one group of parallel (or nearly parallel) dislocations moving on the same slip plane.

As mentioned earlier, the long dislocation arrays, such as array A in Fig. 6b, were found to dominate the dislocation substructure in the S2 alloy containing a high nitrogen concentration. This suggests that these dislocations play a major role in the plastic flow behaviour of the S2 alloy. The results shown in Table VI, suggest that this type of dislocation is nearly screw in character. However, the aforementioned procedure for determination of dislocation character is based upon the assumption of the elastic isotropy [20], and may not be fully applicable to the present case where the anisotropy ratio $A = 2C_{44}/(C_{11} - C_{12})$ is typically 3.5. To determine the character of these dislocations with a higher confidence, we conducted a computer simulation study of the TEM image of the dislocation a shown in Fig. 6b. The character of the dislocation was determined by comparing and matching the simulated image with the corresponding experimental one. As a part of this work, a computer programme which can be used to generate a simulated image of up to three dislocations and three stacking fault ribbons, based upon the two-beam dynamical image simulation method [20], was developed [8]. The results of the simulation can be displayed and/or printed using the Matlab image simulation software [21].

A high-magnification bright-field experimental image of dislocation a, obtained under the two-beam condition associated with $\boldsymbol{g} = (\bar{1}\,\bar{1}\,1)$, is shown in Fig. 7. By applying the TEM image analysis programme [8], the beam direction and the specimen foil normal were determined, respectively, as $\boldsymbol{B} = [10\,1\,11]$ and $\boldsymbol{F} = [12\,1\,0]$. In addition, the following parameters were determined using the same programme the extinction distance $\xi_g = 28.03$ nm, the normalized deviation parameter $w = 1.035$, the specimen foil thickness $t = 82.4$ nm, the anomalous absorption coefficient $\mathscr{A} = 0.053$. The remaining input data necessary for the simulation of the dislocation image, the Burgers vector, the slip plane, and the dislocation line direction, were defined as follows:

TABLE VI Burgers vector $\boldsymbol{b}$, dislocation line direction u, slip plane SP, and Burgers vector/line direction angle α, for dislocations a, b, c, d, and e shown in Fig. 6b

Dislocation designation	Burgers vector $\boldsymbol{b}$	Line direction u	Slip plane SP	Angel α (deg)
a	$\pm a/2\,[1\,1\,0]$	$[13\,19\,\bar{6}]$	$(\bar{1}\,1\,1)$	18
b	$\pm a/2\,[0\,\bar{1}\,1]$	$[14\,13\,1]$	$(\bar{1}\,1\,1)$	64
c	$\pm a/2\,[1\,0\,\bar{1}]$	$[17\,\bar{2}0\,3]$	$(1\,1\,1)$	68
d	$\pm a/2\,[1\,\bar{1}\,0]$	$[\bar{4}\,18\,\bar{1}]$	$(1\,1\,1)$	33
e	$\pm a/2\,[1\,0\,\bar{1}]$	$[4\,\bar{5}\,1]$	$(1\,1\,1)$	71

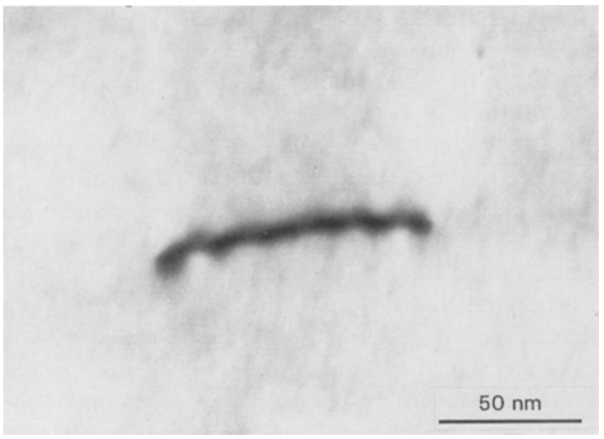

Figure 7 A high-magnification image of the dislocation whose image was simulated, $\boldsymbol{g} = (\bar{1}\,\bar{1}\,1)$, $\boldsymbol{B} = [10\,1\,11]$.

because in the fcc structure, the Burgers vector of a unit dislocation can only be one of the six $\frac{a}{2}\langle 1\,1\,0\rangle$ directions, and the slip plane normal can only be one of the four $\langle 1\,1\,1\rangle$ directions, we assumed that these parameters were determined correctly for dislocation a in Table VI. Consequently, the Burgers vector is set to $\frac{a}{2}[1\,1\,0]$ (the vector sense is not considered because the images of two dislocations differing only in the sense of their Burgers vectors are related by a 180° rotation) and the slip plane normal was taken as $[\bar{1}\,1\,1]$. The dislocation line direction can be in any direction on the slip plane, and therefore has to be determined experimentally. Such determination, however, can be associated with a significant error. Therefore, instead of using the previously determined line direction $[13\,19\,\bar{6}]$ shown in Table VI, the line direction was systematically varied between $[1\,1\,0]$, corresponding to the pure screw dislocation, and $[1\,\bar{1}\,2]$, corresponding to the pure edge dislocation. For brevity, only the simulation results pertaining to the following three special cases are presented here: (a) dislocation a is of the edge type with its line direction $[1\,\bar{1}\,2]$; (b) dislocation a is of the mixed-type with its direction given in Table VI as $[13\,19\,\bar{6}]$; and (c) dislocation a is of the screw type with its line direction $[1\,1\,0]$ parallel to the Burgers vector. The simulation results for these cases corresponding to the same imaging conditions as those associated with the image shown in Fig. 7, are displayed in Fig. 8.

Fig. 7 shows that the experimental image of dislocation a consists of six complete (contrast) oscillations. The dark (dislocation) image on the bright background is continuous and wavy. The simulated image of the edge dislocation, Fig. 8a, is also oscillatory and has six oscillations, but contains discontinuous streaks in the $\sim 150°$ direction rather than being continuous and wavy. Hence, dislocation a is unlikely to be an edge dislocation. In sharp contrast, the simulated images for the nearly screw $[13\,19\,\bar{6}]$ and the screw $[1\,1\,0]$ dislocation displayed, respectively, in Fig. 8b and c, show a much higher resemblance to the experimental image. Taking into account the fact that in the simulations, the dislocation is assumed to be straight while in the actual specimen, the dislocation has some curvature (due to specimen bending, dislocation bow

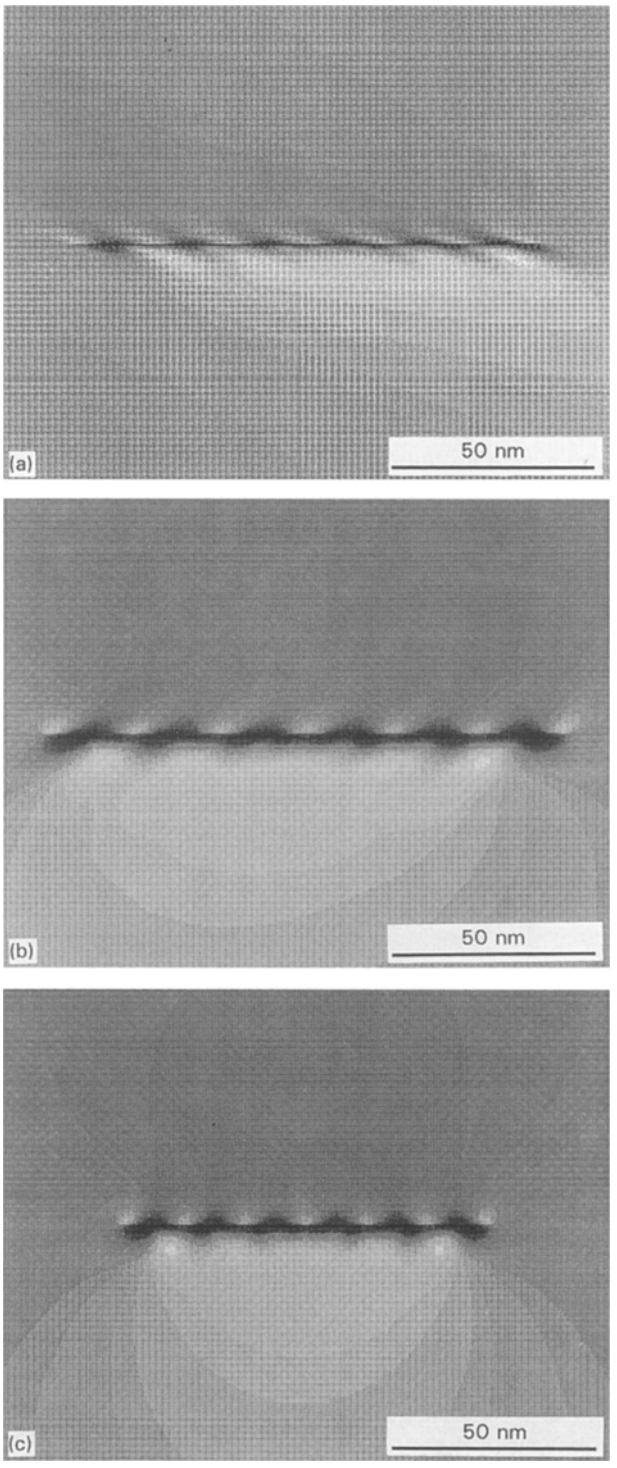

Figure 8 Simulated images of the dislocation shown in Fig. 7. Imaging conditions: $\boldsymbol{g} = (\bar{1}\,\bar{1}\,1]$, $\boldsymbol{B} = [10\,1\,11]$, $\boldsymbol{F} = [12\,1\,0]$, $w = 1.035$, $t = 82.4$ nm; (a) $u = [1\,\bar{1}\,2]$; (b) $u = [13\,19\,\bar{6}]$; and (c) $u = [1\,1\,0]$.

out, etc.), the agreement between Figs 7 and 8b and c is very good. This finding suggests that dislocation a is most likely of screw or nearly screw type, and is consistent with the results of our analysis of the Burgers vector and dislocation line direction shown in Table VI. It should also be noted that no major changes in the simulated image of the $[1\,1\,0]$ screw dislocation were obtained when it was assumed that this dislocation dissociates into two Shockley partials separated by an 8 nm stacking fault ribbon.

It should be noted that the comparison between the simulated images, Fig. 8b and c, and the experimental result, Fig. 7, can be used to determine the sense of the Burgers vector of dislocation a. Recalling that the images of two dislocations differing only in the sense of their Burgers vectors are related by a 180° rotation, the good agreement between the simulated and experimental images in Fig. 8b and c and Fig. 7 suggests that the Burgers vector of dislocation a is $\boldsymbol{b} = \frac{a}{2}[1\,1\,0]$. The sense of the Burgers vector could not be determined by using solely the dislocation invisibility criteria discussed earlier in this section.

4. Discussion

The shape of the obstacle profile, Fig. 2, which is governed by the magnitudes of the parameters $p(=0.43)$, and $q(=1.60)$, Table IV, as well as the small values of the activation volume ($<10\,\Omega$) at the highest stress levels, suggest that the rate-controlling mechanism associated with thermal strengthening in the S2 alloy, is the interaction of dislocations with localized misfitting obstacles (apparently nitrogen atoms in the present case). As shown by the TEM study of the dislocation structure, Fig. 6, the dislocations in this alloy are predominantly screw in character, which implies that the screw dislocations are less mobile than the edge dislocations and hence control the plastic flow behaviour in the S2 alloy. This finding is consistent with our atomistic simulation results [8, 10] which show that nitrogen gives rise to a non-planar dissociation of the core of a screw dislocation, and hence makes it practically sessile. On the contrary, no major changes in the core of an edge dislocation were observed, i.e. the core remains planar, making the edge dislocation very mobile. It is well established that the dislocations in the f c c materials move by the nucleation and the lateral propagation of the kinks [16]. Our atomistic simulation study [8, 10], showed that the interaction of the edge-type kinks formed along a straight screw dislocation with the nitrogen atoms, gives rise to an obstacle profile with the activation parameters $p = 1.00$ and $q = 1.57$ and with an activation volume $V < 40\,\Omega$. Because these results are comparable with their respective counterparts obtained in the present experimental work, it appears that the interaction of nitrogen atoms with the edge kinks is most likely the rate-controlling thermally activated mechanism of dislocation motion in the S2 alloy containing a large concentration of nitrogen.

For the S1 alloy containing a small concentration of nitrogen, the experimental obstacle profile parameters $p = 1.08$ and $q = 1.43$ (Table IV), agree well with $p = 1$ and $q = 1.5$ as predicted by the continuum analysis of the dislocation motion by formation of double kinks over the primary Peierls barrier [16]. These results are also in a good agreement with our atomistic simulation results, $p = 0.86 - 0.87$, and $q = 1.37$, for the double-kink formation process [10]. This implies that the formation of double kinks over the primary Peierls barrier is, most likely, the rate-controlling mechanism for dislocation motion in the Fe–Ni–Cr alloys containing a small concentration of nitrogen. This finding is consistent with the larger values of the activation volume found in the alloy with a smaller nitrogen concentration, Fig. 2. That is, the activation volume is inversely proportional to the height of the Peierls energy barrier [16], and the latter is quite low in the alloy with a low nitrogen concentration.

In our recent atomistic simulation study on the interaction of nitrogen with dislocations [10], the athermal strengthening was found to be the result of the interaction between nitrogen atoms and the stacking fault ribbon of a dissociated dislocation. After accounting for the fact that due to a pinning effect of the nitrogen atoms on the dislocation, the effective nitrogen concentration felt by the dislocation is higher than the nominal one, the athermal component of the shear stress at 298 K was determined as $\tau_a|_{298\,K} = 67.2$ MPa. This value is in a reasonable agreement with the experimental athermal shear stress at 298 K, $\tau_a|_{298\,K} = 52.8$ MPa, obtained for the S2 alloy. In the S1 alloy, the athermal stress is lower, $\tau_a|_{298\,K} = 44.0$ MPa, and this implies that the presence of nitrogen increases the athermal stress, while, as pointed earlier, not affecting significantly the shear modulus of the alloy.

The shear stress versus shear strain curves of the two single crystalline alloys shown in Fig. 4 clearly show the elastic and the plastic deformation stages. The latter stage extends to large shear strains ($\sim 170\%$). Associated with the extended shear strain range of the two shear stress versus shear strain curves in Fig. 4 is a quite small rate of strain hardening (~ 1 MPa/1% shear strain) in the two alloys. This finding can be easily understood, because owing to the absence of the grain boundaries, the motion of dislocations is less inhibited, and because of the small thickness of the tensile specimens, the dislocations can readily move out of a single crystalline specimen. Therefore, the rate of strain hardening which is controlled by the dislocation/dislocation interactions is expected to be low in single crystalline materials, as confirmed by the present results.

The experimental TEM results obtained in the present work, Figs 5 and 6 and Table VI, show that the addition of nitrogen promotes the formation of parallel screw dislocations, forming dislocation arrays (e.g. dislocation array A in Figure 6a). As mentioned earlier, the predominance of the screw dislocations can be related to their lower mobility compared with that of the edge dislocations. In other words, because of their higher mobility, the edge dislocations quickly move out of the crystal while the screw dislocations are left behind. In addition, the higher mobility of the edge component of a mixed dislocation can cause it to convert into a screw dislocation.

The results shown in Fig. 6b and Table VI also indicate that few dislocations, such as dislocations c and e, are nearly edge type. Because such dislocations are exclusively found in the region where two or more dislocation arrays intersect with each other, the long dislocation array, we believe that they are related to the edge kinks formed along the screw dislocations as discussed above.

The observed planar slip in the S2 alloy containing a large concentration of nitrogen, is consistent with the short-range order interstitial strengthening model proposed by Grujicic and Owen [11]. Within the model, the strengthening is attributed to the partial destruction of the local atomic order involving interstitial nitrogen atoms, when a dislocation moves over the slip plane. Owing to the disorder created by the first dislocation, the stress required to move the second dislocation on the same slip plane is lower. Other trailing dislocations encounter progressively lower resistence to their motion, and this promotes planar slip. The short-range order strengthening model further predicts a drop in the stress versus strain curve at the onset of plastic deformation and a lower strain-hardening rate in single crystalline alloys containing a high nitrogen concentration. Our experimental results shown in Fig. 4, however, do not show any evidence of either a stress drop or a lower strain-hardening rate for the S2 alloy. These discrepancies are discussed below.

It should be noted that although the first dislocation destroys the local short-range order and reduces the frictional shear stress for the trailing dislocations, it also repels the trailing dislocations, and hence opposes their motion. The effect of dislocation repulsion becomes particularly important when the leading dislocation is blocked or becomes sessile. Our atomistic simulation results [8, 10] revealed that nitrogen may cause a non-planar dissociation of the core of the screw dislocations, rendering them sessile. Under such conditions, dislocation repulsion may become significant and prevent a drop in stress at the onset of plastic deformation, or a lower strain hardening from occurring in the single crystalline alloys containing a high nitrogen concentration, such as the S2 alloy used in the present work.

The observation of parallel dislocations moving on the same slip plane was previously reported in the polycrystalline Fe–Ni–Cr–N alloys [1, 3–7], but not in single crystals. Formation of a dislocation array or pile-up is generally believed to be the result of a blockage of the leading dislocation in the array by a grain boundary which causes a pile up of the trailing dislocations. However, in single crystalline materials, there are no grain boundaries, and the formation of a dislocation pile-up is not common. Formation of (screw or nearly screw) dislocation pile-ups in the single crystalline S2 alloy containing a high nitrogen concentration implies that the leading dislocation is either blocked by its interaction with the dislocations of another array whose slip plane crosses the slip plane of the former array, and/or it becomes sessile due to some changes in the dislocation core. The TEM results, Fig. 6a–e, provide evidence for the former mechanism of dislocation pile-up formation, while our atomistic simulation results [8, 10] showed that nitrogen can cause the screw dislocation core to dissociate into a non-planar configuration and become sessile.

5. Conclusions

Based upon the experimental results of the tensile tests and the TEM examination of the dislocation character and substructure in the single crystalline Fe–Ni–Cr austenitic alloys containing traces and a high concentration of nitrogen, the following conclusions can be drawn.

1. Nitrogen makes both athermal and thermal contributions to the strength of the single crystalline Fe–Ni–Cr–N austenite.
2. Lower mobility of the screw dislocations compared with the edge dislocations in the alloy with nitrogen, which was predicted by the atomistic simulation of the interaction of dislocations with nitrogen atoms [8], is most likely the cause for the predominant occurrence of screw or nearly screw dislocations in the alloy.
3. The rate-controlling thermally activated mechanism of plastic deformation in the Fe–Ni–Cr austenite containing nitrogen, is the interaction of edge-type kinks formed along the sessile screw dislocations with nitrogen atoms. In contrast, thermally activated nucleation of double kinks over the primary Peierls barrier appears to be the rate-controlling mechanism for the plastic flow in the Fe–Ni–Cr austenite without nitrogen.
4. The absence of the stress drop at the onset of yielding, and the absence of a lower strain-hardening rate as predicted by the short-range order strengthening model, can be attributed to the repulsive interaction between parallel dislocations gliding on the same plane.

Acknowledgements

This work was supported by the National Science Foundation under Grant DMR-9102973. The authors are indebted to Dr Bruce A. MacDonald, NSF, for encouragement and continuing interest in this work. We also thank Professor Walter S. Owen, MIT, for constant support and friendship.

References

1. M. L. G. BYRNES, M. GRUJICIC and W. S. OWEN, *Acta Metall.* **35** (1987) 1853.
2. J. -O. NILSSON and T. THORVALDSSON, *Scand. J. Metall.* **15** (1985) 83.
3. M. GRUJICIC, J. -O. NILSSON, W. S. OWEN, and T. THORVALDSSON, "International Conference on High Nitrogen Steels", edited by J. Foct and A. Hendry, HNS-88 Lille, France (The Institute of Metals, London, 1989) p. 154.
4. J. RAWERS, G. ASAI, R. DOAN and J. DUNNING, *J. Mater. Res.* 7 (1992) 1083.
5. J. SASSEN. A. J. GARRATT-REED, and W. S. OWEN, in "International Conference on High Nitrogen Steels", edited by J. Foct and A. Hendry, HNS-88 Lille, France (The Institute of Metals, London, 1989) p. 135.
6. J. -O. NILSSON, *Scripta Metall.* **17** (1983) 593.
7. J. -O. NILSSON, *Fatigue Eng. Matter. Struct.* 7 (1984) 55.
8. X. W. ZHOU, PhD Dissertation, Clemson University, USA (1995).
9. M. GRUJICIC and X. W. ZHOU, *Mater. Sci. Eng.* (1995) submitted.
10. *Idem. ibid.* **A190** (1995) 87.
11. M. GRUJICIC and W. S. OWEN, *Calphad* **16** (1992) 291.
12. R. D. LEGGETT, R. E. REED and H. W. PAXTON, *Trans. Metall. Soc. AIME* **215** (1959) 679.
13. B. SUNDMAN, private communication (1994).
14. P. GRIEVESON and E. T. TURKDOGAN, *Trans. Metall. Soc. AIME* **230** (1964) 407.

15. E. SCHMID and W. BOAS, "Plasticity of Crystals", (Hughes, London, 1950) p. 57.
16. U.F. KOCKS, A. S. ARGON and M.F. ASHBY, *Progr. Mater. Sci.* **19** (1975) 1.
17. W. S. OWEN and M. GRUJICIC, in "Encyclopedia of Materials Science and Engineering", edited by M. B. Bever (Pergamon Press, Oxford, 1986) p. 3540.
18. G. THOMAS and M. J. GORINGE, "Transmission Electron Microscopy of Materials", (Wiley, New York, 1979) p. 1.
19. P. B. HIRSCH, A. HOWIE, P. B. NIGHOLSON, D. W. PASHLEY and M. J. WHELAN, "Electron Microscopy of Thin Crystals" (Butterworths, London, 1965) p. 1.
20. A. K. HEAD, P. HUMBLE, L. M. CLAREBROUGH, A. J. MORTON and C. T. FORWARD, in "Defects in Crystalline Solids: Computed Electron Micrographs and Defect Identification", edited by S. Amelinckx, R. Gevers, and J. Nihoul (North-Holland, Amsterdam, 1973) p. 1.
21. MATLAB, The Math Works, Inc. (1992).

Received 12 May
and accepted 1 December 1995